Analysis of Thermal–Hydraulic Behavior during Loss-of-Coolant Accidents in PWR Plants for Pressurized Thermal Shock Assessment

Hideki Yagihashi[a], Naofumi Tsukamoto[b]
[a]Nuclear Regulation Authority (NRA), Tokyo, Japan, *yagihashi_hideki_w3p@nra.go.jp*
[b]Nuclear Regulation Authority (NRA), Tokyo, Japan, *tsukamoto_naofumi_dz5@nra.go.jp*

Abstract: As nuclear power plants transition to long-term operation, neutron-irradiation-induced embrittlement of reactor pressure vessels (RPVs) has emerged as a critical safety issue. During a loss-of-coolant accident (LOCA) in a pressurized water reactor (PWR), the emergency core cooling system (ECCS) injects cold water into the RPV, causing the RPV wall to cool rapidly. This process can generate considerable thermal stresses in the wall, which may be superimposed on the pressure-induced membrane stresses. This phenomenon, known as pressurized thermal shock (PTS), may compromise the integrity of the RPV, particularly when pre-existing flaws exist within RPV walls subjected to substantial neutron-irradiation-induced embrittlement, thereby warranting rigorous assessment.
PTS assessment methodologies have been advancing from deterministic approaches based on conservative conditions toward probabilistic fracture mechanics (PFM) approaches grounded in more realistic plant behavior. The thermal–hydraulic conditions for PTS scenarios for deterministic assessment are conservative, whereas PFM employs realistic input conditions and probabilistic evaluations with statistical treatment of uncertainties. In PFM assessments, it is essential to employ realistic thermal–hydraulic conditions and explicitly characterize the associated uncertainties.
Herein, to obtain fundamental insights supporting the application of PFM methodology to PTS assessment, we investigated LOCA events (one of the principal initiators of PTS) using a four-loop PWR plant model developed with the TRACE thermal–hydraulic code. Two selected LOCA scenarios were analyzed to characterize the system responses, with particular emphasis on the detailed thermal–hydraulic behavior within the RPV downcomer during ECCS injection, where this region and the associated processes are central to PTS assessment.

1. INTRODUCTION

In the long-term operation of nuclear power plants, the reactor pressure vessel (RPV) experiences progressive neutron irradiation embrittlement, making the structural integrity of the RPV a safety-significant issue. In Japan, the number of nuclear power plants operating for >40 years is increasing, and accordingly, evaluating pressurized thermal shock (PTS) has become increasingly important. PTS occurs when the injection of emergency core cooling water, associated with events such as a loss-of-coolant accident (LOCA), rapidly cools the region near the inner-wall surface of the RPV. The simultaneous action of large temperature gradients and internal pressure results in high tensile stresses near the RPV inner-wall surface.

PTS assessment encompasses material degradation owing to neutron irradiation and loads induced by rapid cooling. Regarding the latter, two key issues exist from the thermal–hydraulic perspective. One is how hot and cold water mix in the cold leg (CL) and the downcomer (DC), which has been investigated experimentally and analytically [1,2,3,4]. The other is plant behavior in sequences that can lead to PTS, which serves as a direct input for PTS assessment. Systematic studies of plant behavior have been conducted in the United States [5,6,7], and more recently, benchmark analyses have been conducted in the European APAL project [8].

Traditionally, the structural integrity of the RPV against PTS has been evaluated using deterministic fracture mechanics, assuming conservative conditions. However, in the United States and elsewhere, efforts have been made to enhance PTS assessment by applying probabilistic fracture mechanics (PFM)

[9,10,11,12]. PTS assessments using PFM generally account for location-dependent neutron fluence based on the neutron-flux distribution. By contrast, evaluations of the cooling behavior of the RPV wall have not sufficiently accounted for thermal–hydraulic spatial dependence; thus, uncertainties arising from this limitation persist.

Therefore, herein, to reduce thermal–hydraulic uncertainties in PTS assessment, focus was placed on the spatial dependence of the evolution of cooling in the RPV wall, and plant thermal–hydraulic analyses were performed under LOCA conditions. In particular, a four-loop PWR analysis model using the TRACE code developed by the U.S. NRC [13] was employed, and two scenarios were defined for a CL 5-inch break LOCA: one with a high-pressure injection system (HPI) available and the other with an HPI unavailable. Through these analyses, focus was placed on the thermal–hydraulic behavior in the DC region during emergency core cooling system (ECCS) water injection. Considering the overall system behavior, the evolution of cooling in the RPV wall was qualitatively characterized and the impact on PTS assessment was discussed.

2. TRACE ANALYSIS OF 4-LOOP PWR PLANT

2.1. Analytical Model

Figure 1 shows the TRACE four-loop PWR analysis model used in this study. The major design specifications of the analytical model are summarized in Table 1. Among the four loops, the valve components are modeled in the CL and hot leg (HL) of Loop 1 to simulate a pipe break. In addition, in Loop 3, a valve component is modeled to simulate a break in the surge line (SRG) connected to the pressurizer. The RPV is modeled using a VESSEL component. In this study, loops other than the broken loop are referred to as intact loops.

Figure 2 presents the details of the RPV modeled using the VESSEL component. The RPV is modeled as a cylindrical structure and is divided into 5 radial, 4 azimuthal, and 18 axial segments. The DC, which is important for PTS evaluation, is located in the outermost cylindrical region ($r = 5$) and is assigned to the axial segments from the third to the sixteenth segments, counted from the bottom among the 18 axial divisions. Furthermore, within the DC region, the axial active fuel region height with high neutron fluence, the so-called beltline region [14], corresponds to the axial segments from the fourth to the eleventh segments, counted from the bottom. In addition, the nozzle elevation is located at the fourteenth axial segment counted from the bottom among the 18 axial divisions.

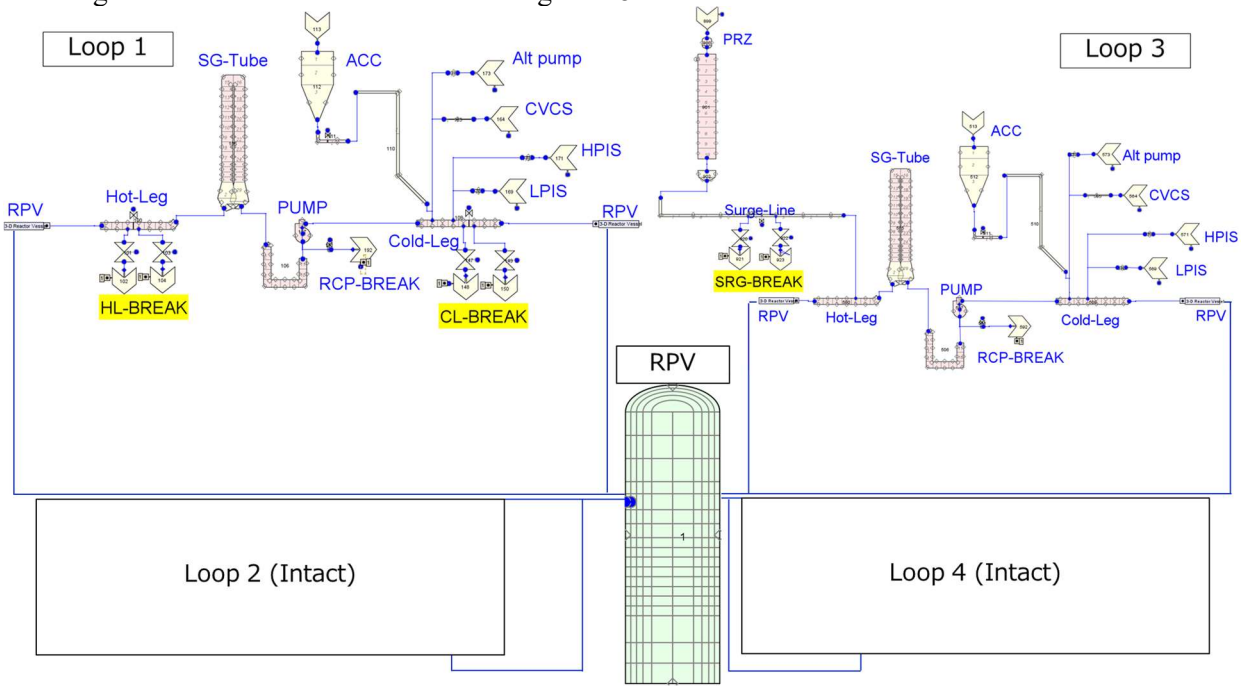

Fig.1. Node Diagram of TRACE Analytical Model of 4-loop PWR

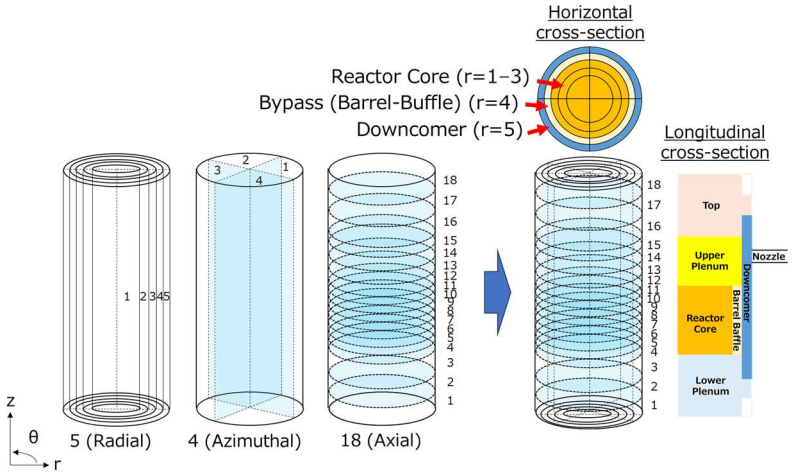

Fig.2. TRACE Analytical Model of 4-loop PWR (RPV)

Table 1: Design Parameters for PWR Model

Core power (MW)	3423
Primary pressure (MPa)	15.5
Primary coolant average temperature (K)	580
Primary coolant temperature (low-temperature side) (K)	562
Primary coolant temperature (high-temperature side) (K)	598
HPI coolant temperature (K)	303
Accumulator (ACC) coolant temperature (K)	322
Low-pressure injection system (LPI) coolant temperature (K)	303
Core height (m)	3.65
DC height (m)	8.60
Number of fuel rods	50952

2.2 Scenarios Selected for Analysis

From the perspective of reducing thermal–hydraulic uncertainties in PTS assessment, Table 2 summarizes the thermal–hydraulic analyses for LOCA scenarios for a four-loop PWR currently being conducted, with the objective of obtaining a comprehensive understanding of the effects of ECCS conditions and break size and location. In this study, among these LOCA scenarios, the scenarios with available and unavailable HPI for a 5-inch CL break were selected as targets for analysis for the following reasons.

Reason for selecting a CL break: Because ECCS water is injected into the CL, when a break occurs, an outflow of ECCS water from the opening of the break is expected. Consequently, ECCS water inflow into the RPV differs for the intact versus broken loops. This enables the evaluation of azimuthal anisotropy in the thermal–hydraulic behavior in the DC region caused by these differences.

Reason for selecting a 5-inch break: In the case of a 5-inch break, the primary system pressure does not immediately decrease to full depressurization after the break, and a high-pressure condition is maintained for a certain period. At the same time, the DC water level changes significantly depending on the ECCS water-injection mode. Therefore, differences in the evolution of cooling behavior in the DC wall resulting from different ECCS injection modes tend to become pronounced, making this break size appropriate for evaluating differences in the cooling behavior of the DC wall that are important for PTS assessment.

Reason for selecting HPI available and unavailable scenarios: The availability or unavailability of HPI significantly impacts the DC water level during the LOCA progression. When HPI is unavailable, the DC water level decreases, and low-temperature accumulator (ACC) injection water may flow in while the wall surface is exposed, potentially causing localized rapid cooling. In contrast, different cooling

behavior is expected when HPI is available. By considering both scenarios, differences in the evolution of cooling in the DC wall and their impact on PTS assessment can be identified.

Regarding the break conditions, the break was modeled by specifying an opening fraction corresponding to a 5-inch break diameter for the valve component simulating the CL break.

Table 2: LOCA Scenarios

Break location	Break size (inch)	ECCS condition
CL	1,5,10	HPI available/unavailable
HL	1,5,10	HPI available/unavailable
SRG	1,5,10	HPI available/unavailable

3. RESULTS AND DISCUSSION

3.1. Results

The present analysis focuses on the DC beltline region (z = 4–11), important for PTS assessment. Figure 3 shows the assignment of different colors to the node elevations in the DC beltline region. In Fig. 4(c,d), Fig. 5(c,d), Fig. 8, Fig. 9, and Fig. 10, the results for the liquid-phase temperature and DC wall temperature are presented using the color coding corresponding to the node elevations shown in Fig. 3.

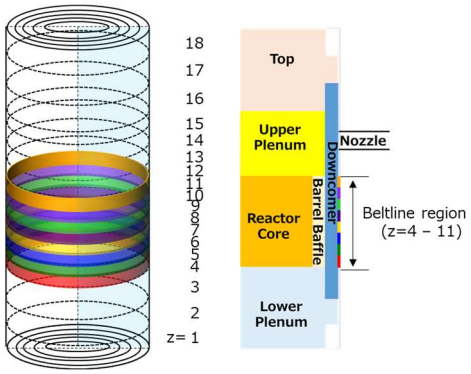

Fig.3. Color Assignment to each Node in the DC Beltline Region

3.1.1 CL 5-inch Break with HPI Available

Figure 4 shows the results for a 5-inch CL break with HPI available. Figure 4(a) presents the rate of ECCS inflow into the CL of the broken loop (θ = 1), specifically those of the HPI (red) and ACC injection systems (blue). Figure 4(b) shows the DC water level, where the froth water level is indicated by a black line and the collapsed water level is shown by a red line. Figure 4(c) shows the liquid-phase temperature in the DC beltline region (z = 4–11) of the broken loop (θ = 1), and Fig. 4(d) shows the wall temperature in the same region. The liquid-phase temperature and wall temperature of the DC beltline region shown in Fig. 4(c), (d) correspond to the color assignment for each node in the DC beltline region shown in Fig. 3. In all figures, the time histories are shown as a function of the elapsed time after break initiation, with the break initiation time set to 0 s.

As shown in Fig. 4(a), HPI starts injection approximately 30 s after the break and maintains a flow rate of 20–30 kg/s. By contrast, ACC starts injection approximately 500 s after the break, where the flow rate into the CL varies in the range of 0–70 kg/s in the broken loop (θ = 1). As shown in Fig. 4(b), neither the froth water level nor the collapsed water level in the DC decreases to the DC beltline region. In this case, the froth and collapsed water levels are almost identical, indicating that no significant two-phase region develops in the DC below the water level.

The data in Fig. 4(c) confirm that the liquid-phase temperature in the DC beltline region remains at the saturation temperature before the start of ACC injection and then transitions to a subcooled condition after ACC injection. As shown in Fig. 4(d), the wall temperature in the DC beltline region follows a trend similar to that of the liquid-phase temperature, remaining near the saturation temperature until approximately 600 s and then becoming subcooled. Overall, the wall temperature remains higher than the liquid-phase temperature and lower than the saturation temperature.

These results suggest that when HPI is available, the DC water level does not decrease to the DC beltline region and this region remains flooded throughout the transient. In addition, the liquid-phase temperature and the wall temperature remain below the saturation temperature. Consequently, the DC wall temperature decreases monotonically according to the decrease in the surrounding liquid-phase temperature.

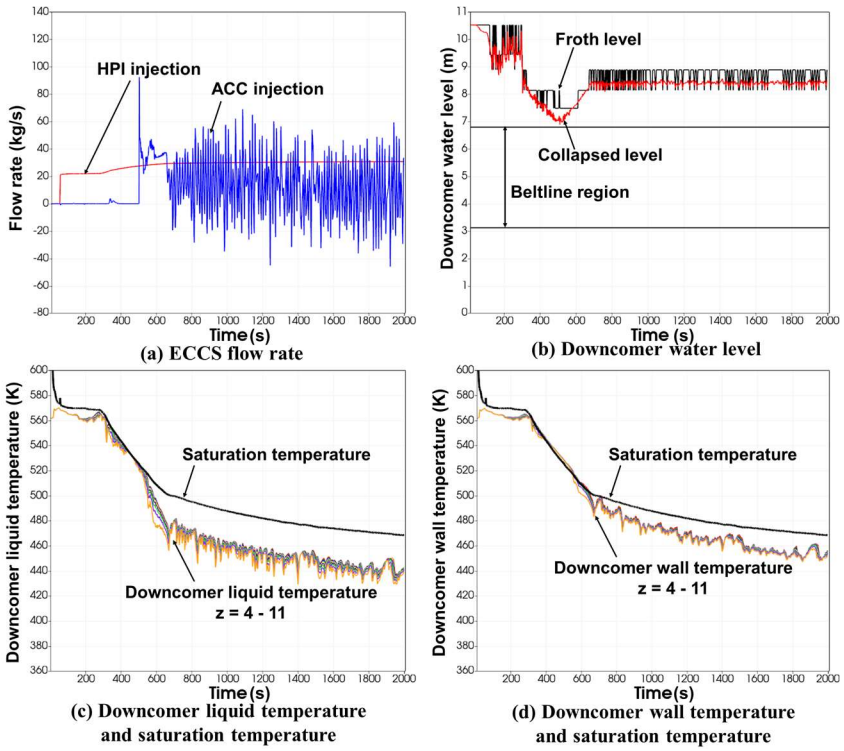

Fig.4. Results for CL 5-inch Break with HPI Available

3.1.2 CL 5-inch Break with HPI Unavailable

Figure 5 shows the results for a 5-inch CL break with HPI unavailable. Figure 5(a) presents the rate of ECCS inflow into the CL of the broken loop (θ = 1), specifically those of HPI (red) and the ACC injection system (blue). Figure 5(b) shows the DC water level, where the froth water level is indicated by a black line and the collapsed water level is marked by a red line. Figure 5(c) shows the liquid-phase temperature in the DC beltline region (z = 4–11) of the broken loop (θ = 1), and Fig. 5(d) shows the wall temperature in the same region. The liquid-phase and wall temperatures of the DC beltline region shown in Fig. 5(c), (d) correspond to the color coding of each node in the DC beltline region shown in Fig. 3.

As shown in Fig. 5(a), because HPI is unavailable, the HPI injection flow rate is 0 kg/s, whereas ACC flows into the CL for periods of 700–1100 s and 1600–1700 s after the break. The ACC flow rate reached a maximum of approximately 60 kg/s in the broken loop (θ = 1). Because of the differential relationship between the primary system pressure and ACC pressure, reverse flow into the ACC system occurred immediately upon terminating injection into the CL, and although brief, negative flow rates were observed.

As shown in Fig. 5(b), the froth water level and the collapsed water level in the DC decreased to the lower part of the DC beltline region at approximately 700 s. Although the water level subsequently

recovered, it did not recover to the upper part of the DC beltline region, and the exposed condition persisted. As shown in Fig. 5(c), the liquid-phase temperature in the DC remained at the saturation temperature throughout the transient, and the froth water level remained higher than the collapsed water level, indicating that the DC was in a froth condition.

As shown in Fig. 5(d), the wall temperature in the upper exposed region of the DC beltline region (z = 6–11) remained near the saturation temperature until approximately 500 s. After 500 s, the wall temperature increased above the saturation temperature, starting from the upper part of the DC beltline region. Subsequently, at approximately 740 s, the wall was rapidly cooled, and the temperature decreased to the saturation temperature, and was maintained until approximately 1100 s. Thereafter, the temperature increased again, followed by another rapid cooling at approximately 1600 s, after which the saturation temperature was maintained until approximately 1730 s. A subsequent temperature increase was observed. By contrast, in the lower nonexposed region of the DC beltline region (z = 4 and z = 5), no temperature increase from the saturation temperature followed by rapid cooling was observed.

These results reveal that as the DC water level decreases, the DC beltline region becomes exposed sequentially from the upper part and the DC wall temperature increases above the saturation temperature in the order of exposure. In addition, rapid cooling of the DC wall occurs slightly later than the start of ACC inflow into the CL (approximately 730 and 1610 s following ACC initiation at approximately 700 and 1580 s, respectively). After rapid cooling, the wall temperature remains at the saturation temperature during ACC injection. Almost simultaneously with the termination of ACC inflow, the wall temperature increases again (approximately 1100 and 1730 s).

From the above, when HPI is unavailable, the DC water level decreases to the lower part of the DC beltline region prior to ACC injection, resulting in exposure of the DC beltline region. The wall temperature in the DC beltline region remains near the saturation temperature until exposure. However, after exposure, it increases sequentially from the upper region and exhibits rapid cooling associated with ACC inflow into the CL. This rapid cooling is observed in correspondence with the timing of the two ACC injections and is crucial for PTS assessment.

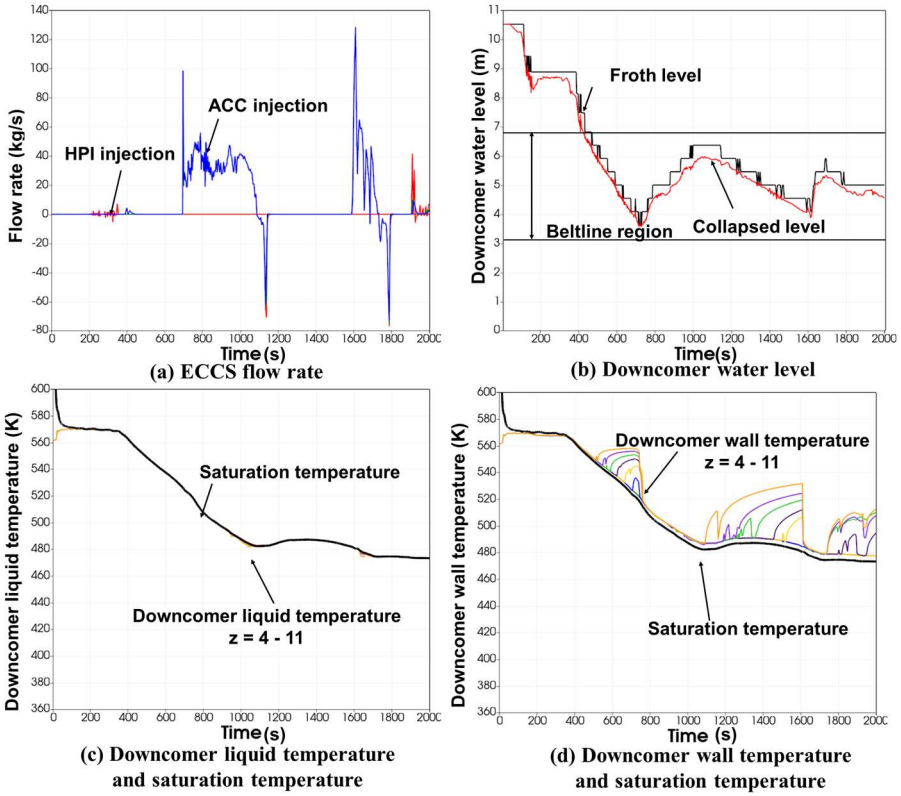

Fig.5. Results for CL 5-inch Break with HPI Unavailable

3.2. Discussion

The results presented in Section 3.1 confirm that even for the same 5-inch CL break, the thermal–hydraulic behavior in the DC of the broken loop considerably differs depending on whether HPI is available or unavailable. Accordingly, this section provides further discussion from the viewpoint of PTS assessment, with emphasis on the differences in the thermal–hydraulic behavior in the DC for the broken versus intact loops as well as the relationship among the DC wall temperature in the DC beltline region, ECCS water injection behavior, and the DC water level.

3.2.1 Azimuthal Differences in Thermal–Hydraulic Behavior in DC

In this section, focus is placed on the azimuthal thermal–hydraulic behavior in the DC region. The discussion highlights differences in the DC wall temperature arising from differences in the evolution of ECCS water inflow into the RPV for the intact versus broken loops, owing to the discharge of ECCS water from the break opening.

(a) CL 5-inch Break with HPI Available

Figure 6 shows the DC wall temperature distributions for the 5-inch CL break with HPI available. In Fig. 6(a), the region to which the DC is assigned in the RPV nodal diagram is indicated in light-blue. Figure 6(b) presents the time-series distributions of the DC wall temperature obtained by unwrapping the DC region into a 360° planar view. When HPI is available (Fig. 4(d)), the wall temperature changes gradually without abrupt variations; therefore, the time series is presented at 400 s intervals.
Azimuthal differences between the broken and intact loops are most pronounced at the nozzle elevation (z = 14). Compared with the intact loops, the DC wall temperature in the broken loop is higher and a persistent difference is observed, attributable to delayed cooling owing the discharge of ECCS water from the break opening. In contrast, in the DC beltline region (z = 4–11), no pronounced azimuthal differences between the broken and intact loops, such as those observed at the nozzle elevation, are identified.

(b) CL 5-inch Break with HPI Unavailable

Figure 7 shows the DC wall temperature distributions for the 5-inch CL break with HPI unavailable. In Fig. 7(a), the region assigned as the DC in the RPV nodal diagram is indicated in light-blue. Figure 7(b) presents the time-series distributions of the DC wall temperature in the 360° planar view. When HPI is unavailable (Fig. 5(d)), the wall temperature is characterized by two rapid cooling events (~750 s and ~1600 s). Accordingly, the time series focuses on the periods before and after these rapid cooling events, and the results are shown at 700 s and 800 s and at 1600 s and 1700 s.

Regarding azimuthal differences between the broken and intact loops, no pronounced differences were observed at 700 s and 1600 s, i.e., before the rapid cooling events. By contrast, at 800 s and 1700 s, i.e., after the rapid cooling events, pronounced azimuthal differences were observed at the nozzle elevation (z = 14). In the DC beltline region (z = 4–11), although distinct azimuthal differences between the broken and intact loops, such as those observed at the nozzle elevation, were not identified, axial temperature differences were observed at 700 s and 1600 s, before the rapid cooling events.

Overall, for the 5-inch CL break LOCA, pronounced azimuthal temperature differences in the DC wall were observed at the nozzle elevation in both the HPI available and unavailable cases, attributable to ECCS water discharge from the break. These azimuthal temperature non-uniformities are considered characteristic of CL break scenarios, whereas they are less likely for HL breaks without ECCS discharge. In contrast, no significant azimuthal temperature differences were identified in the DC beltline region. In the HPI unavailable case, axial temperature differences were also observed, suggesting more complex thermal–hydraulic behavior associated with variations in the DC water level and the resulting exposure of the DC wall during the transient. Accordingly, the complex axial behavior observed in the HPI unavailable case is further analyzed in the following section.

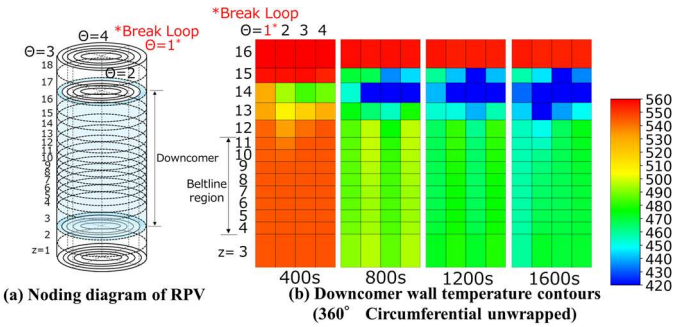

Fig.6. DC wall Temperature Distribution for CL 5-inch Break with HPI Available

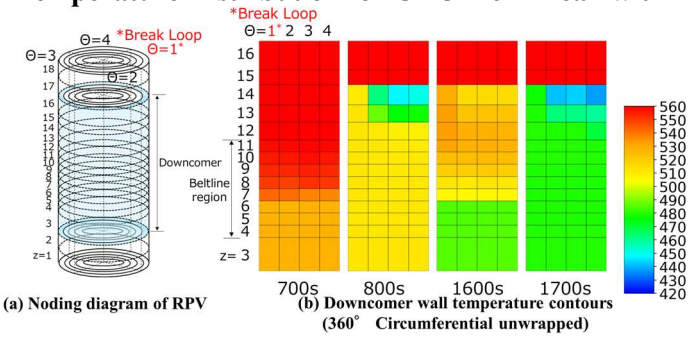

Fig.7. DC Wall Temperature Distribution for CL 5-inch Break with HPI Unavailable

3.2.2 Relationship between Beltline Wall Temperature, DC Water level, and ACC Flow Rate

This section focuses on the temperature increase associated with exposure of the DC wall and the subsequent two rapid cooling events observed for the 5-inch CL break with HPI unavailable. The cooling modes governing these behaviors are examined in detail. In particular, causal relationships underlying the rapid cooling behavior are clarified by comparing the relationship between the DC water level and the DC beltline region wall temperature and the relationship between the ACC flow rate and the wall temperature for the broken and intact loops. In addition, the cooling rate ($\Delta T/\Delta t$) during each rapid cooling event is evaluated to quantitatively assess the cooling behavior.

(a) Broken Loop

Figure 8(a) shows the relationship between the wall temperature in the DC beltline region and the ACC flow rate and inflow rate into the RPV for Loop 1 ($\theta = 1$), which is the broken loop. Figure 8(b) shows the relationship between the wall temperature in the DC beltline region and the DC water level.

As shown in Fig. 8(a), the timing of rapid cooling of the DC wall nearly coincides with the onset of inflow into the RPV (approximately 740 s). After rapid cooling, the wall temperature in the DC beltline region is maintained near the saturation temperature during inflow into the RPV, as indicated by the two arrows in the figure. Regarding the timing relationship between the start of ACC injection and the onset of inflow into the RPV, a time lag of approximately 50 s (around 690 and 740 s) is observed for the first peak, whereas a time lag of approximately 20 s (around 1590 and 1610 s) is observed for the second peak. In addition, a difference of approximately one-half between the ACC injection flow rate and the inflow rate into the RPV is identified for both the first and second peaks (approximately 40 and 20 kg/s, and 60 and 30 kg/s, respectively).

As shown in Fig. 8(b), during the first temperature rise of the DC beltline region wall (500–750 s), the DC water level decreases, and the individual nodes become exposed sequentially from the upper part of the beltline region. For all nodes, the wall temperature begins to increase approximately 40 s after exposure. Although the DC water level recovers twice, it does not reach the elevation of the uppermost node of the DC beltline region; the uppermost node remains exposed from approximately 470 s until the end of the transient. In contrast, the lowermost node of the DC beltline region remains submerged throughout the transient and is never exposed. The first rapid cooling of the DC wall temperature

(approximately 740 s) occurs slightly later than, but nearly coincides with, the start of recovery of the DC water level (approximately 710 s). Similarly, the timing of the second rapid cooling of the DC wall temperature (approximately 1600 s) almost coincides with the onset of recovery of the DC water level.

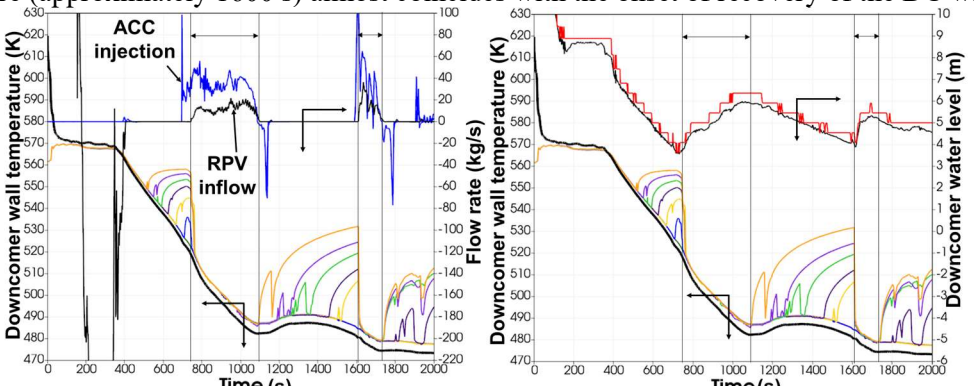

(a) Downcomer wall temperature and ECCS flow rate - RPV inflow rate

(b) Downcomer wall temperature and downcomer water level

Fig.8 Thermal–Hydraulics in the Broken Loop of the 5-inch CL Break with HPI Unavailable

(b) Intact Loop

Figure 9(a) shows the relationships between the wall temperature in the DC beltline region and the ACC flow rate and the inflow rate into the RPV for Loop 2 ($\theta = 2$), which is an intact loop. Figure 9(b) shows the relationship between the wall temperature in the DC beltline region and the DC water level.
As shown in Fig. 9(a), the start time of ACC injection and the start time of ACC water inflow into the RPV nearly coincide, and the rapid cooling of the DC wall coincides with the onset of ACC water inflow into the RPV (approximately 710 s). After rapid cooling, the wall temperature in the DC beltline region remains near the saturation temperature during inflow into the RPV, as indicated by the two arrows in the figure. Note that at the first peak, the ACC injection flow rate into the primary system and the ACC water inflow rate into the RPV are of nearly the same order (approximately 40 and approximately 60 kg/s, respectively).

As shown in Fig. 9(b), during the first increase in the wall temperature of the DC beltline region (approximately 500–700 s), the DC water level decreases, and the individual nodes become exposed sequentially from the upper part. For all nodes, the wall temperature starts to increase approximately 40 s after exposure. The uppermost node of the DC beltline region becomes exposed from the DC water level at approximately 470 s and remains exposed until the end of the transient. In contrast, the lowermost node of the DC beltline region remains submerged throughout the transient and is never exposed. The timing of the first rapid cooling of the DC wall temperature (approximately 705 s) nearly coincides with the start of recovery of the DC water level (approximately 710 s). In addition, recovery of the DC water level is almost simultaneous with the second rapid cooling of the DC wall temperature (approximately 1600 s).

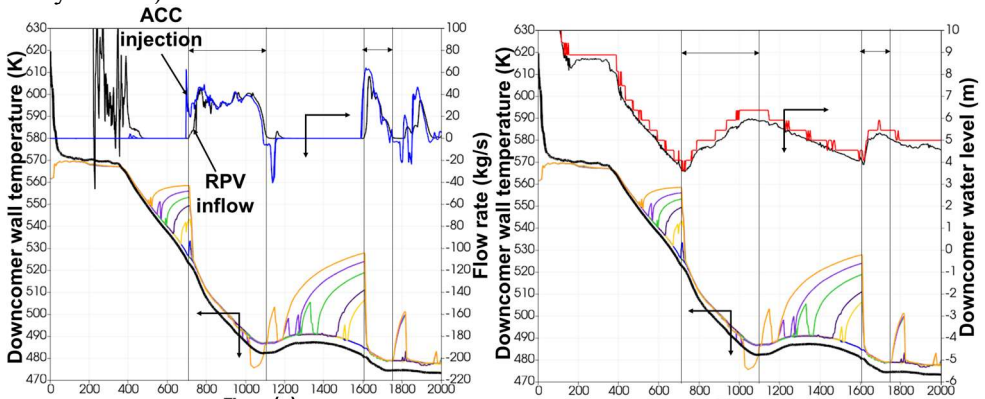

(a) Downcomer wall temperature and ECCS flow rate - RPV inflow rate

(b) Downcomer wall temperature and downcomer water level

Fig.9 Thermal–Hydraulics in the Intact Loop of 5-inch CL Break with HPI Unavailable

(c) Relationship between DC Water Level and DC Wall Temperature

The inflow rate of ACC water into the RPV and the start time of inflow differed significantly in the broken versus intact loops. In the broken loop, a portion of the ACC water is discharged through the break opening, reducing the effective inflow rate into the RPV to approximately half that in the intact loops, and delaying the inflow start time by approximately 50 s.

From Fig. 8 and Fig. 9, the overall increase in the wall temperature is generally similar in both the intact and broken loops. The wall temperature increases in the region z = 6–11 within the DC beltline region (z = 4–11). In these regions, rapid cooling is almost simultaneous with the start of inflow into the RPV, and the wall temperature remains near the saturation temperature during inflow. When inflow into the RPV is terminated, the wall temperature again increases, starting from the upper side (z = 11).

In contrast, in the lower regions (z = 4 and z = 5), no wall-temperature increase was observed, and the temperature remained near the saturation temperature throughout the transient. This suggests that in the upper part of the DC beltline region, where the exposure time is relatively long, cooling owing to ACC water inflow into the RPV is the dominant cooling mechanism, whereas in the lower region, where the exposure time is short or exposure does not occur, cooling by water retained in the DC plays a dominant role.

From the above, it is confirmed that even within the DC beltline region (z = 4–11), the dominant cooling mode differs for the lower region (z = 4, 5) versus upper region (z = 6–11).

3.2.3 Cooling Rate of DC Wall Temperature at Rapid Cooling Points

In this section, the cooling rates associated with the two rapid cooling events observed for the 5-inch CL break with HPI unavailable are derived. Figure 10 shows the locations in the DC beltline region wall where rapid cooling occurs in the broken loop, Loop 1 (θ = 1).

For the first rapid cooling event, a temperature decrease of 35.3 K occurred over 16.4 s at the uppermost node of the DC beltline region (z = 11), corresponding to a cooling rate of $\Delta T/\Delta t$ = 2.14 K/s. For the second rapid cooling event, a temperature decrease of 44.5 K occurred over 10.1 s at the same location (z = 11), yielding a cooling rate of $\Delta T/\Delta t$ = 4.39. K/s.

Similarly, the cooling rates associated with rapid cooling events in the intact loops (Loops 2–4) were evaluated. The results are summarized in Table 3, and the relationship between temperature decrease and cooling duration is illustrated in Fig. 11, showing that temperature drops of 30–50 K occurred repeatedly with cooling rates of up to approximately 4 K/s.

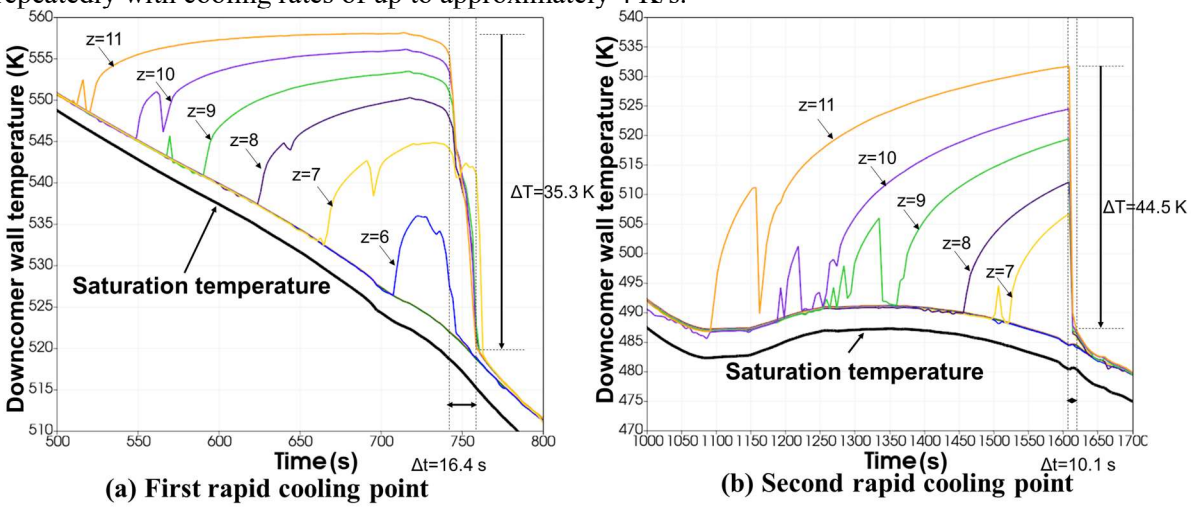

(a) First rapid cooling point (b) Second rapid cooling point

Fig.10. Temperature Decrease and Duration in DC Wall at Rapid Cooling Points in the Broken Loop

Table 3: Cooling Rate ($\Delta T/\Delta t$) in Each Loop

	First, rapid cooling			Second rapid cooling		
	Δt (s)	ΔT (K)	$\Delta T/\Delta t$	Δt (s)	ΔT (K)	$\Delta T/\Delta t$
Loop 1 (Broken)	16.5	35.3	2.14	10.1	44.5	4.39
Loop 2 (Intact)	18.4	32.7	1.78	10.1	40.8	4.03
Loop 3 (Intact)	22.5	34.0	1.51	10.1	41.9	4.13
Loop 4 (Intact)	18.3	31.8	1.74	10.1	40.7	4.02

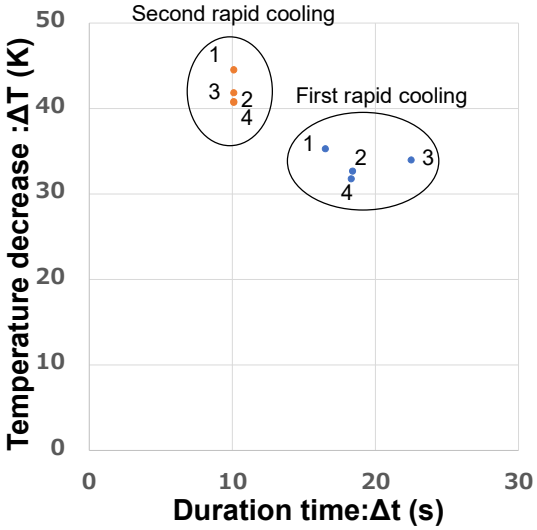

Fig.11. Cooling Rate ($\Delta T/\Delta t$) of DC Wall at Rapid Cooling Points

4. CONCLUSION

Herein, plant thermal–hydraulic analyses under LOCA conditions were performed for a four-loop PWR with the objective of reducing uncertainties in PTS assessment associated with the spatial and temporal evolution of DC wall cooling. Focusing on the evolution of rapid cooling under high-pressure conditions, which directly affects thermal boundary conditions for PTS evaluation, a 5-inch CL break LOCA was selected and two scenarios were considered: HPI available and HPI unavailable. Considering the overall system behavior, emphasis was placed on analyzing the thermal–hydraulic behavior in the DC region from the viewpoint of providing realistic input conditions for PFM-based PTS assessment.

The principal findings of this study are as follows:

(1) Even under the same 5-inch CL break condition, the thermal–hydraulic behavior in the DC region differs considerably, depending on the availability of HPI. When HPI is unavailable, the DC water level decreases to the lower part of the DC beltline region before ACC inflow, resulting in exposure of the DC beltline region. The wall temperature in the DC beltline region remains near the saturation temperature until exposure; after exposure, it increases sequentially from the upper region and then decreases sharply at the timing of ACC water injection. This rapid cooling behavior was observed at the timing of the two ACC injections.

(2) With respect to azimuthal distributions of the DC wall temperature, pronounced differences were observed at the nozzle elevation both in the HPI available and HPI unavailable cases, whereas no considerable azimuthal differences were identified in the DC beltline region.

(3) Notably, when HPI is unavailable, a cooling mode is identified in which ACC injection water directly flows into the exposed DC beltline region wall (z = 6–11), inducing steep and localized cooling. As a result of these thermal–hydraulic processes, the DC wall undergoes rapid cooling events, with temperature decreases of 30–50 K observed multiple times, with cooling rates of up to approximately 4 K/s.

The study results indicate that the DC wall cooling behavior varies depending on the ECCS operating conditions. This finding implies that, when applying PFM to PTS assessment using thermal–hydraulic analysis results for individual LOCA scenarios as inputs, the branching associated with ECCS operating modes needs to be explicitly considered.

For the rapid cooling behavior of the DC wall observed in this study, the quantitative assessment of its significance in PTS evaluation remains an issue for future work.

Acknowledgements

The authors sincerely thank Prof. Abe for his insightful discussions and constructive advice on thermal-hydraulics and two-phase flow that were essential to the present work.

References

[1] H. Tuomisto and P. Mustonen, *"Thermal Mixing Tests in a Semi-Annular Downcomer with Interacting Flows from Cold Legs,"* U.S. Nuclear Regulatory Commission, NUREG/IA-0004, 1986.
[2] T. Höhne and S. Kliem, "Numerical Analysis Related to the ROCOM Pressurized Thermal Shock Benchmark," *Fluids*, vol. 8, no. 1, p. 4, 2022.
[3] M. Aghazarian, Ts. Malakyan, A. Nalbandyan, and A. Amirjanyan, *"CFD Modeling of Mixing Phenomena for Pressurized Thermal Shock Analysis on the Downcomer of WWER-440,"* Proceedings of NURETH-16, 2015.
[4] T. Höhne, S. Kliem, H.-M. Prasser, and U. Rohde, *"Experimental and Numerical Mixing Studies Inside a Reactor Pressure Vessel,"* Proceedings of the ASME/JSME 2003 4th Joint Fluids Engineering Conference, FEDSM2003-45294, pp. 1211–1222, 2003.
[5] W. C. Arcieri, R. M. Beaton, C. D. Fletcher, and D. E. Bessette, *"RELAP5 Thermal-Hydraulic Analysis to Support PTS Evaluations for the Oconee 1, Beaver Valley 1, and Palisades Nuclear Power Plants,"* U.S. Nuclear Regulatory Commission, NUREG/CR-6858, Sep. 2004.
[6] Y. H. Chang, K. Almenas, A. Mosleh, and D. Bessette, *"Thermal-Hydraulic Uncertainty Analysis in the Context of Pressurized Thermal Shock Risk Scenarios,"* in Probabilistic Safety Assessment and Management, A. Spitzer et al., Eds., Springer, London, 2004, pp. 1816–1825.
[7] U.S. Nuclear Regulatory Commission, *"Technical Basis for Revision of the Pressurized Thermal Shock (PTS) Screening Limit in the PTS Rule (10 CFR 50.61): Summary Report,"* NUREG-1806, Vol. 1, Aug. 2007.
[8] APAL Consortium, *"Work Package 2 – Improvement of Thermal-Hydraulic Analysis: Quantification of Uncertainties in TH Analysis Related to Computer Code Models, Plant Parameters and Human Factors,"* Public Summary Report 2, European Commission Horizon 2020 Programme, 2024.
[9] B. R. Bass, C. E. Pugh, J. Sievers, and H. Schulz, *"International Comparative Assessment Study of Pressurized Thermal Shock in Reactor Pressure Vessels,"* U.S. Nuclear Regulatory Commission, NUREG/CR-6651, 1999.
[10] U.S. Nuclear Regulatory Commission, *"Probabilistic Fracture Mechanics – Models, Parameters, and Uncertainty Treatment Used in FAVOR Version 04.1,"* NUREG-1807, 2007.
[11] U.S. Nuclear Regulatory Commission, *"Sensitivity Studies of the Probabilistic Fracture Mechanics Model Used in FAVOR,"* NUREG-1808, 2010.
[12] U.S. Nuclear Regulatory Commission, *"Technical Basis for the Use of Probabilistic Fracture Mechanics in Regulatory Applications: Final,"* NUREG/CR-7278, 2022.
[13] U.S. Nuclear Regulatory Commission, TRACE V5.0 Theory Manual: Field Equations, Solution Methods, and Physical Models, 2008.
[14] International Atomic Energy Agency, Pressurized Thermal Shock in Nuclear Power Plants: Good Practices for Assessment, IAEA-TECDOC-1627, Vienna, 2010.